

Equivariant Evidential Deep Learning for Interatomic Potentials

Zhongyao Wang ^{*1 2 3} Taoyong Cui ^{*2 4} Jiawen Zou ¹ Shufei Zhang ² Bo Yan ¹ Wanli Ouyang ^{2 4}
Weimin Tan ^{†1} Mao Su ^{†2 5}

Abstract

Uncertainty quantification (UQ) is critical for assessing the reliability of machine learning interatomic potentials (MLIPs) in molecular dynamics (MD) simulations, identifying extrapolation regimes and enabling uncertainty-aware workflows such as active learning for training dataset construction. Existing UQ approaches for MLIPs are often limited by high computational cost or suboptimal performance. Evidential deep learning (EDL) provides a theoretically grounded single-model alternative that determines both aleatoric and epistemic uncertainty in a single forward pass. However, extending evidential formulations from scalar targets to vector-valued quantities such as atomic forces introduces substantial challenges, particularly in maintaining statistical self-consistency under rotational transformations. To address this, we propose *Equivariant Evidential Deep Learning for Interatomic Potentials* (e²IP), a backbone-agnostic framework that models atomic forces and their uncertainty jointly by representing uncertainty as a full 3×3 symmetric positive definite covariance tensor that transforms equivariantly under rotations. Experiments on diverse molecular benchmarks show that e²IP provides a stronger accuracy-efficiency-reliability balance than the non-equivariant evidential baseline and the widely used ensemble method. It also achieves better data efficiency through the fully equivariant architecture while retaining single-model inference efficiency.

1. Introduction

Machine-learning interatomic potentials (MLIPs) enable large-scale molecular dynamics (MD) by approximating *ab initio* potential energy surfaces at dramatically reduced cost (Behler & Parrinello, 2007). With recent advances in $E(3)$ -equivariant neural architectures, MLIPs can now achieve near first-principles accuracy for energies and atomic forces, substantially extending the accessible time- and length-scales of atomistic simulation and supporting a broad range of applications from materials property prediction to non-equilibrium processes (Batzner et al., 2022; Batatia et al., 2022; Thomas et al., 2018; Gasteiger et al.; Wood et al., 2025; Musaelian et al., 2023). As a result, MLIPs are becoming a key tool for bridging first-principles modeling and large-scale atomistic simulation (Jia et al., 2020; Kozinsky et al., 2023).

Despite these advances, deploying MLIPs reliably in long-timescale MD remains challenging (Perez et al., 2025). Even small force errors can accumulate over millions of integration steps, leading to unphysical trajectories and unreliable conclusions (Fu et al.). Reliable and computationally efficient uncertainty quantification (UQ) is therefore essential for safe deployment (Bilbrey et al., 2025), as well as for uncertainty-aware workflows such as data selection and adaptive model refinement.

Ensembles are widely used and often regarded as a robust “gold standard” for UQ in MLIPs (Gal & Ghahramani, 2016; Lakshminarayanan et al., 2017; Wollschläger et al., 2023; Willow et al., 2025), but their training and inference costs scale linearly with the number of models, making them expensive for large-scale simulation. Moreover, recent work has raised concerns about the calibration reliability of ensembles in certain settings (Rahaman et al., 2021; Abe et al., 2022; Dern et al., 2024). These limitations motivate single-model UQ approaches that provide uncertainty estimates in a single forward pass. Evidential deep learning (EDL) is a promising direction: by predicting parameters of a prior distribution, it enables direct estimation of both aleatoric and epistemic uncertainty within one pass (Sensoy et al., 2018; Amini et al., 2020; Deng et al., 2023). However, most existing EDL methods target scalar properties (Soleimany et al., 2021). Xu et al. proposed an evidential interatomic

¹College of Computer Science and Artificial Intelligence, Fudan University, Shanghai, China ²Shanghai Artificial Intelligence Laboratory, Shanghai, China ³Shanghai Innovation Institution, Shanghai, China ⁴The Chinese University of Hong Kong, Hong Kong SAR, China ⁵Shenzhen Institute of Advanced Technology, Chinese Academy of Sciences, Shenzhen, China. Correspondence to: Weimin Tan <wmtan@fudan.edu.cn>, Mao Su <sumao@pjlab.org.cn>.

potential (eIP) (Xu et al., 2025) for forces, but models uncertainty as independent per-axis variances in a fixed global frame (i.e., a diagonal covariance). While this can express axis-aligned anisotropy, it cannot capture cross-axis correlations (off-diagonal structure) that are often necessary in vector-valued error modeling. More critically, without a full tensor structure, uncertainty cannot transform consistently under rigid rotations, which breaks the coherence of the probabilistic scale and undermines the stability of uncertainty-based ranking decisions across orientations.

Rotation consistency is fundamental for vector-valued force prediction. Forces are equivariant vectors: under a rotation R , the target transforms as $\mathbf{F} \mapsto R\mathbf{F}$. When adopting a probabilistic EDL framework for uncertainty modeling, consistency requires not only an equivariant mean prediction but also a distributional structure that transforms accordingly. By basic statistical transformation rules, if a random vector satisfies $\mathbf{Y}' = R\mathbf{Y}$, then its covariance must satisfy $\Sigma' = R\Sigma R^\top$. Therefore, in EDL frameworks where uncertainty is represented by covariance tensors, equivariance of uncertainty is not an additional physical assumption but a requirement for distributional self-consistency.

Motivated by this observation, we propose *Equivariant Evidential Deep Learning for Interatomic Potentials* (e²IP), an equivariant evidential framework for vector-valued force prediction (Fig. 1). e²IP represents force uncertainty as a full 3×3 symmetric positive definite (SPD) covariance tensor, capturing directional structure and cross-axis correlations while remaining consistent under rotation, and retaining single forward pass efficiency. To guarantee strict positive definiteness and rotation-consistent covariance construction, we parameterize a symmetric matrix in the Lie algebra and map it to the SPD manifold via the matrix exponential. Built on a Normal–Inverse–Wishart (NIW) evidential model, e²IP naturally decomposes uncertainty into aleatoric and epistemic components. To ensure numerical robustness in complex energy landscapes and long-timescale MD, we further introduce equivariance-preserving spectral stabilization and evidence regularization to mitigate overconfidence and prevent numerical degeneracy. Experiments on diverse molecular benchmarks demonstrate that e²IP achieves a better balance of accuracy, efficiency, and reliability compared to baseline methods, providing a practical and physically consistent framework for uncertainty-aware molecular simulations.

Contributions.

- We introduce e²IP, an $SO(3)$ -equivariant evidential framework that models aleatoric and epistemic uncertainty in vector-valued forces as full 3×3 SPD covariances in a single forward pass.
- We propose an $SO(3)$ -consistent full-covariance construction via a Lie-algebra parameterization and matrix exponential, together with equivariance-preserving spectral stabilization for numerically robust training.

- Through extensive validation across diverse molecular benchmarks, e²IP demonstrates better uncertainty calibration and data efficiency at the single-model inference cost.

2. Preliminaries

Problem setup. We consider an atomic configuration \mathcal{G} with atomic coordinates $\{\vec{x}_i \in \mathbb{R}^3\}_{i=1}^N$ and atomic species $\{z_i \in \mathbb{Z}\}_{i=1}^N$. Our goal is to predict the atom-wise vector-valued property $\{\vec{y}_i \in \mathbb{R}^3\}_{i=1}^N$, such as the force acting on atom i , while simultaneously estimating the uncertainty associated with each atomic prediction. Within the evidential deep learning framework, the uncertainty for each atom is represented by a 3×3 covariance matrix.

Equivariant backbone features. We assume an $SE(3)$ -equivariant backbone f_θ (e.g., NequIP (Batzner et al., 2022), MACE (Bataia et al., 2022)) that maps \mathcal{G} to node-wise latent features organized in irreducible representation (irrep) spaces. For each atom i , the backbone outputs a collection of irrep-valued features $\{\mathbf{h}_i^l\}$, including scalars ($l = 0$) and higher-order tensors ($l > 0$). These features will later be used by task-specific heads to produce both the predictive mean and an uncertainty estimate.

2.1. Equivariance requirements for mean and covariance

Let $g = (R, \mathbf{t}) \in SE(3)$, where R is an orthogonal matrix with $\det(R) = 1$ and $\mathbf{t} \in \mathbb{R}^3$. Since atomic forces are translation-invariant, physical consistency requires the predicted target to transform as a vector:

$$\vec{y}_i(g \cdot \mathcal{G}) = R \vec{y}_i(\mathcal{G}). \quad (1)$$

The uncertainty associated with a vector prediction is represented by a symmetric positive definite (SPD) rank-2 tensor $\Sigma_i \in \mathbb{S}_{++}^3$ (e.g., a covariance or scale matrix). Rotation consistency then requires

$$\Sigma_i(g \cdot \mathcal{G}) = R \Sigma_i(\mathcal{G}) R^\top. \quad (2)$$

In particular, predicting independent per-axis variances (a diagonal matrix in a fixed global basis) generally violates Eq. (2) under non-trivial rotations and cannot capture anisotropic correlations aligned with local geometric directions.

2.2. Irrep structure of symmetric rank-2 tensors

Any symmetric matrix $\mathbf{S}_i \in \mathbb{S}^3$ admits an orthogonal decomposition into an isotropic trace component and a traceless

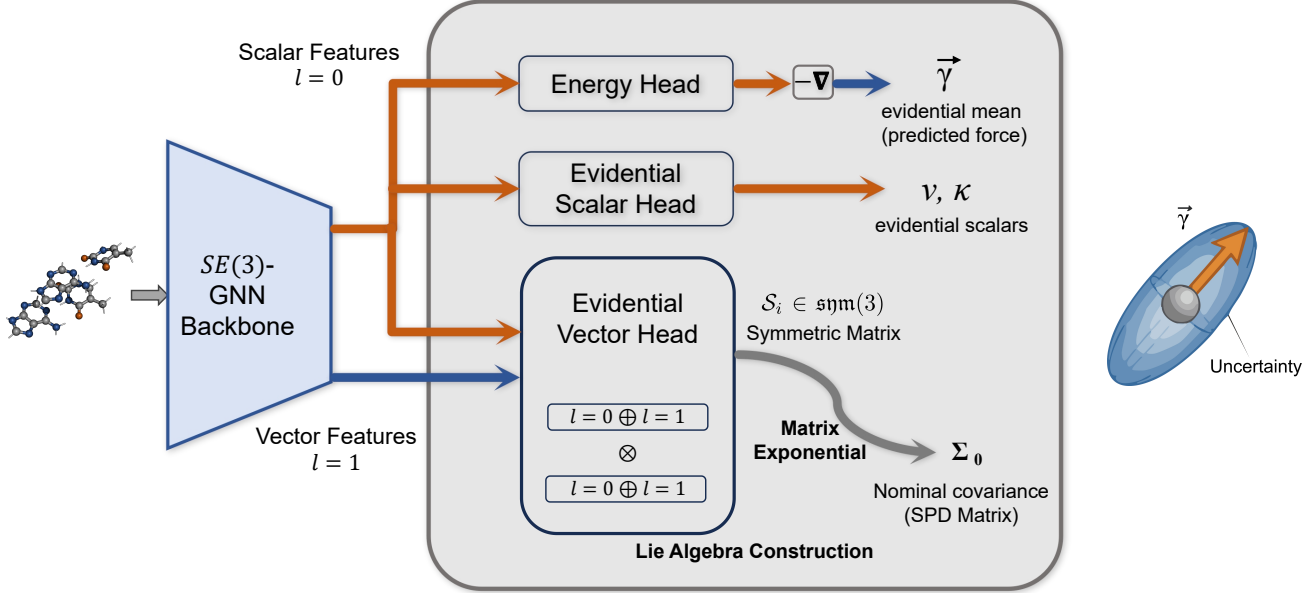


Figure 1. $e^2\text{IP}$ framework. An $SE(3)$ -equivariant GNN predicts the force mean and NIW evidential parameters, and constructs an equivariant SPD covariance Σ_0 (via a symmetric-matrix Lie-algebra head and matrix exponential) to produce tensor-valued uncertainty in a single forward pass.

symmetric component:

$$\mathbf{S}_i = \underbrace{\frac{1}{3}\text{tr}(\mathbf{S}_i)\mathbf{I}}_{0e} + \underbrace{\left(\mathbf{S}_i - \frac{1}{3}\text{tr}(\mathbf{S}_i)\mathbf{I}\right)}_{2e}. \quad (3)$$

From the viewpoint of $SO(3)$ representation theory, the space of symmetric rank-2 tensors decomposes as $(0e \oplus 2e)$: the scalar $(0e)$ channel corresponds to the trace, and the five-dimensional $(2e)$ channel corresponds to the traceless symmetric part. This structure provides a natural, rotation-compatible parameterization for constructing \mathbf{S}_i (and hence $\Sigma_{0,i}$) from equivariant features.

3. Methodology

Overview. We propose *Equivariant Evidential Deep Learning for Interatomic Potentials* ($e^2\text{IP}$), a single forward pass probabilistic framework for atom-wise vector regression with rotation-consistent uncertainty (Fig. 1). Given an input structure, an $SE(3)$ -equivariant network jointly predicts the force mean and a *full* 3×3 SPD uncertainty tensor for each atom. Uncertainty is modeled using a Normal–Inverse–Wishart (NIW) evidential formulation, yielding a multivariate Student- t predictive distribution with explicit aleatoric and epistemic decomposition. The method is built on two key components: (i) an equivariant SPD covariance construction via a symmetric-matrix (Lie algebra) parameterization and matrix exponential, and (ii) an equivariance-preserving spectral stabilizer that bounds covariance scale during training, ensuring strict SPD validity, rotation consistency, and numerical stability for full-covariance learning.

For completeness, we summarize all symbols and validity conditions in Appendix B.

3.1. Multivariate Evidential Learning Framework

We model the observation \vec{y}_i with a Gaussian likelihood whose mean and covariance are latent:

$$p(\vec{y}_i | \vec{\mu}_i, \Sigma_i) = \mathcal{N}(\vec{y}_i | \vec{\mu}_i, \Sigma_i). \quad (4)$$

Following multivariate evidential regression (Meinert & Lavin, 2021), we place a Normal–Inverse–Wishart (NIW) prior over $(\vec{\mu}_i, \Sigma_i)$:

$$\Sigma_i \sim \mathcal{W}^{-1}(\Psi_i, \nu_i), \quad \vec{\mu}_i | \Sigma_i \sim \mathcal{N}\left(\vec{\gamma}_i, \frac{1}{\kappa_i} \Sigma_i\right). \quad (5)$$

Physically interpretable scale parameterization. To obtain an interpretable scale matrix from the network, we reparameterize

$$\Psi_i \triangleq \nu_i \Sigma_{0,i}, \quad (6)$$

where $\Sigma_{0,i} \in \mathbb{S}_{++}^3$ is an SPD matrix and describes the *shape* of the aleatoric noise (up to a scalar factor controlled by ν_i).

Posterior predictive. Marginalizing $(\vec{\mu}_i, \Sigma_i)$ yields a multivariate Student- t predictive distribution:

$$p(\vec{y}_i | \vec{\gamma}_i, \Sigma_{0,i}, \nu_i, \kappa_i) = \text{St}_{m_i}(\vec{y}_i | \vec{\gamma}_i, \Lambda_i), \quad (7)$$

$$m_i \triangleq \nu_i - d + 1, \quad \Lambda_i \triangleq \frac{\nu_i(\kappa_i + 1)}{\kappa_i(\nu_i - d + 1)} \Sigma_{0,i}.$$

A full derivation and the expanded negative log-likelihood are given in Appendix C.

Aleatoric and epistemic uncertainty decomposition. The NIW hierarchy induces an uncertainty decomposition:

$$\begin{aligned}\mathbf{U}_{\text{ale}} &\triangleq \mathbb{E}[\Sigma_i] = \frac{\nu_i \Sigma_{0,i}}{\nu_i - d - 1} \\ \mathbf{U}_{\text{epi}} &\triangleq \text{Var}[\vec{\mu}_i] = \frac{1}{\kappa_i} \mathbb{E}[\Sigma_i] = \frac{\nu_i \Sigma_{0,i}}{\kappa_i(\nu_i - d - 1)}\end{aligned}\quad (8)$$

\mathbf{U}_{ale} reflects observation noise, while \mathbf{U}_{epi} captures uncertainty in the mean induced by limited data, and both terms transform equivariantly under rotations when $\Sigma_{0,i}$ does.

Constraints and stable scalar parameterization. We require $\kappa_i > 0$ and $\nu_i > d + 1$ so that $\mathbb{E}[\Sigma_i]$ exists in Eq. (8). In practice we enforce a stronger lower bound $\nu_i \geq d + 2$ to avoid the near-singular regime of $\nu_i/(\nu_i - d - 1)$. We enforce constraints via shifted softplus:

$$\begin{aligned}\nu_i &= \text{softplus}(\hat{\nu}_i) + (d + 2) \\ \kappa_i &= \text{softplus}(\hat{\kappa}_i) + \epsilon\end{aligned}\quad (9)$$

where $\epsilon = 10^{-6}$.

3.2. Equivariant SPD covariance via Lie algebra

A central challenge is predicting $\Sigma_{0,i} \in \mathbb{S}_{++}^3$ while preserving rotation equivariance ($\Sigma_{0,i} \mapsto R\Sigma_{0,i}R^\top$). Standard parameterizations (e.g., Cholesky) can be implementation-dependent and may break equivariance.

Lie-algebra to SPD via matrix exponential. We predict coefficients in the irreducible representation space ($0e \oplus 2e$), map them to a Cartesian symmetric matrix $\mathcal{S}_i \in \mathfrak{sym}(3)$, and define

$$\Sigma_{0,i} = \exp(\mathcal{S}_i). \quad (10)$$

Because \mathcal{S}_i is symmetric, it admits an eigen-decomposition $\mathcal{S}_i = U\Lambda U^\top$ with real eigenvalues; hence $\exp(\mathcal{S}_i) = U \exp(\Lambda) U^\top$ has strictly positive eigenvalues and is therefore SPD. Moreover, the matrix exponential is conjugation-equivariant: for any $R \in SO(3)$,

$$\exp(R\mathcal{S}_i R^\top) = R \exp(\mathcal{S}_i) R^\top, \quad (11)$$

which follows from the power-series definition of $\exp(\cdot)$ and the identity $(R\mathcal{S}_i R^\top)^k = R\mathcal{S}_i^k R^\top$. Consequently, $\Sigma_{0,i}$ transforms equivariantly as a rank-2 tensor. (Shumaylov et al.)

Irrep-to-Cartesian map. Let $\mathbf{z}_i = [s_i, \mathbf{t}_i] \in \mathbb{R}^{1+5}$ denote the predicted coefficients, where s_i is the $l = 0$ channel and \mathbf{t}_i parameterizes the $l = 2$ (symmetric traceless) channel. We use a fixed linear map to obtain $\mathcal{S}_i \in \mathfrak{sym}(3)$; details (including the constant map \mathbf{Q} and vectorization convention) are provided in Appendix D.

3.3. Spectral stabilization via coefficient-space damping

While Eq. (10) guarantees geometric validity, large-magnitude \mathcal{S}_i may lead to ill-conditioned $\Sigma_{0,i}$ due to the exponential growth/shrinkage of eigenvalues. To stabilize training without explicit eigendecomposition, we damp the coefficients in representation space before constructing \mathcal{S}_i .

Equivariance-preserving damping. For the scalar channel, we apply a smooth two-sided damper $\tilde{s}_i = \phi_{\text{low}}(\phi_{\text{high}}(s_i))$. For the $l = 2$ channel, we damp only the magnitude:

$$\tilde{\mathbf{t}}_i = \alpha_i \mathbf{t}_i, \quad \alpha_i \triangleq \frac{\phi_{\text{high}}(\|\mathbf{t}_i\|_2)}{\|\mathbf{t}_i\|_2 + \epsilon}. \quad (12)$$

Since $\|\mathbf{t}_i\|_2$ is rotation-invariant, α_i is invariant, and the operation preserves equivariance by construction. We then form $\tilde{\mathbf{z}}_i = [\tilde{s}_i, \tilde{\mathbf{t}}_i]$, map it to \mathcal{S}_i , and compute $\Sigma_{0,i} = \exp(\mathcal{S}_i)$. The explicit piecewise linear-Tanh form of $\phi_{\text{high}}/\phi_{\text{low}}$ is provided in Appendix E.

3.4. Training objective

The evidential model outputs a nominal covariance $\Sigma_{0,i}$ and two evidence parameters (ν_i, κ_i) , optimized by maximum likelihood estimation with a regularization term.

Student-*t* negative log-likelihood. Minimizing the negative log-likelihood of Eq. (7) yields the training loss in Eq. (13). For completeness, the expanded form used in the implementation is reported in Appendix C.

$$\begin{aligned}\mathcal{L}_{\text{NLL},i} &= \log \Gamma\left(\frac{\nu_i - d + 1}{2}\right) - \log \Gamma\left(\frac{\nu_i + 1}{2}\right) \\ &\quad + \frac{d}{2} \log\left(\frac{\pi \nu_i (1 + \kappa_i)}{\kappa_i}\right) + \frac{1}{2} \log |\Sigma_{0,i}| \\ &\quad + \frac{\nu_i + 1}{2} \log\left(1 + \frac{\kappa_i}{\nu_i(1 + \kappa_i)} \mathbf{M}\right).\end{aligned}\quad (13)$$

$$\mathbf{M} \triangleq (\vec{y}_i - \vec{\gamma}_i)^\top \Sigma_{0,i}^{-1} (\vec{y}_i - \vec{\gamma}_i)$$

Evidence regularization. To discourage overconfident evidence on hard or out-of-distribution samples, we add a monotonic penalty on evidence:

$$\mathcal{L}_{\text{reg},i} = (\nu_i + \kappa_i) \|\vec{y}_i - \vec{\gamma}_i\|_2, \quad (14)$$

and optimize $\mathcal{L}_{\text{total}} = \mathcal{L}_{\text{NLL}} + \lambda \mathcal{L}_{\text{reg}}$. Note that $\partial \mathcal{L}_{\text{reg}} / \partial \nu_i = \|\vec{y}_i - \vec{\gamma}_i\|_2$, so larger errors induce a stronger gradient opposing evidence accumulation.

Scalar proxy for tensor epistemic uncertainty. For comparison against scalar error metrics, we report

$$u_{\text{scalar}} = \sqrt{\text{tr}(\mathbf{U}_{\text{epi}})/3}. \quad (15)$$

Algorithm 1 Forward and loss on atom i

- 1: $\{\mathbf{h}_i^\ell\} \leftarrow f_\theta(G)$, {SE(3)-equivariant backbone}
- 2: $\mathbf{E} \leftarrow \text{EnergyHead}(\{\mathbf{h}_i^0\})$, {energy}
- 3: $\gamma_i \leftarrow -\nabla \mathbf{E}$, {vector mean}
- 4: $(\hat{\nu}_i, \hat{\kappa}_i) \leftarrow \text{MLP}(\mathbf{h}_i^0)$
- 5: $\nu_i \leftarrow \text{softplus}(\hat{\nu}_i) + (d+2)$; $\kappa_i \leftarrow \text{softplus}(\hat{\kappa}_i) + \epsilon$
- 6: $(s_i, \mathbf{t}_i) \leftarrow \text{EquivariantHead}(\{\mathbf{h}_i^\ell\})$, {0e \oplus 2e coeffs}
- 7: $(\tilde{s}_i, \mathbf{t}_i) \leftarrow \text{Damp}(s_i, \mathbf{t}_i)$
- 8: $S_i \leftarrow \text{SymMap}([\tilde{s}_i, \mathbf{t}_i]) \in \text{sym}(3)$
- 9: $\Sigma_{0,i} \leftarrow \exp(S_i)$
- 10: Compute $\mathcal{L}_{\text{NLL},i}$
- 11: Compute $\mathcal{L}_{\text{reg},i}$
- 12: Compute $\mathcal{L}_{\text{energy}}$
- 13: $\mathcal{L}_{i,\text{forces}} \leftarrow \mathcal{L}_{\text{NLL},i} + \lambda_{\text{reg}} \mathcal{L}_{\text{reg},i}$
- 14: **Return** $\mathcal{L}_i \leftarrow \lambda_{\text{energy}} \mathcal{L}_{i,\text{energy}} + \lambda_{\text{forces}} \mathcal{L}_{i,\text{forces}}$

The trace is rotation-invariant ($\text{tr}(R\mathbf{A}R^\top) = \text{tr}(\mathbf{A})$), providing a consistent scalar summary.

4. Experiments

We evaluate e²IP across molecular dynamics benchmarks to characterize both predictive performance and the usability of its uncertainty estimates. Specifically, we study (i) probabilistic reliability and calibration on *ab initio* liquid water against a deep ensemble baseline, (ii) sample efficiency and geometric consistency on supramolecular MD22 systems with non-equivariant evidential baselines and an equivariance ablation, (iii) generalization under distribution shift and backbone migration on the Out of Distribution (OOD) SILICA glass benchmark, and (iv) numerical robustness of full-covariance learning via spectral-stabilization ablations. Unless otherwise stated, we use AlphaNet (Yin et al., 2025) as the *SE(3)*-equivariant backbone.

4.1. Evaluation on *Ab Initio* Liquid Water Thermodynamics

We evaluate e²IP on the *ab initio* liquid water benchmark of Cheng *et al.* (Cheng et al., 2019) (revPBE0-D3). Liquid water is a demanding condensed-phase setting: strong anharmonic fluctuations and nuclear quantum effects induce substantial, configuration-dependent variability in atomic forces. This benchmark stress-tests whether UQ remains *reliable and actionable* under realistic physical noise, i.e., whether predicted confidence levels agree with empirical frequencies which is a prerequisite for uncertainty-aware workflows such as risk control in long-timescale molecular dynamics, anomaly screening, and ranking decisions in active learning.

We use an 80%/10%/10% train/validation/test split and report mean \pm std over five random seeds. We compare

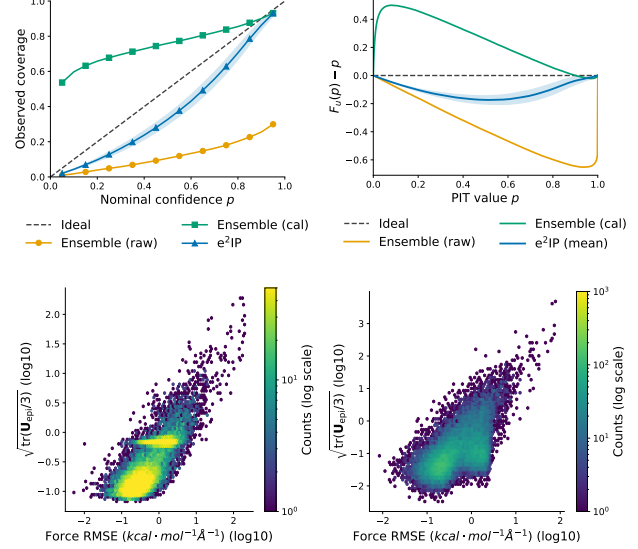


Figure 2. Uncertainty diagnostics on liquid water. Top-left: reliability diagram (observed vs. nominal coverage; dashed line is ideal). Top-right: PIT CDF deviation $\hat{F}_U(p) - p$ (zero is ideal). Ensemble (raw) is strongly overconfident, while post-hoc calibration over-corrects and becomes under-confident; e²IP stays closest to the ideal in both views. Bottom: alignment between force error and predicted epistemic scale, plotting Force RMSE against $\sqrt{\text{tr}(\mathbf{U}_{\text{epi}}/3)}$ (both in log10), shown as 2D density (counts in log scale) for e²IP (left) and Ensemble (right). e²IP exhibits a clearer monotonic relationship and higher Spearman correlation (0.78 vs. 0.61), indicating better error-aware ranking.

against an ensemble baseline consisting of five independently trained models with different random seeds, reporting both its raw output (Ensemble(raw)) and a post-hoc calibrated variant (Ensemble(cal)). The calibration fits a single isotropic scale σ^2 on the validation set to target ~ 0.9 coverage and is fixed for test evaluation (Appendix G).

We report point accuracy (Force MAE), probabilistic quality (Energy Score, ES (Gneiting & Raftery, 2007); negative log-likelihood, NLL), and calibration diagnostics (Coverage@95, Calibration Error, CE, and PIT; Fig. 2) (Table 1). While ES and NLL are both proper scoring rules, NLL is more sensitive to overconfident failures and distributional mis-scaling, whereas ES emphasizes average multivariate distribution matching. PIT assesses distributional calibration: a calibrated model yields uniform PIT values, hence $\hat{F}_U(p) - p \approx 0$. The results show a clear accuracy-efficiency-reliability trade-off: the ensemble achieves lower MAE via model averaging but incurs substantially higher inference latency, while e²IP attains competitive accuracy with a single forward pass and yields an approximately 4.5 \times per-atom speedup, which is crucial for large-scale or long-timescale simulations.

More importantly, probabilistic and calibration metrics re-

Table 1. Results on the ab initio liquid water benchmark (Cheng et al., 2019). We report Force MAE (lower is better), Energy Score (ES, lower is better), Coverage@95 (closer to 0.95 is better), Calibration Error (CE, lower is better), Negative log-likelihood (NLL, lower is better), and inference time per atom (ms; lower is better). All numbers are mean \pm std over five random seeds. For the ensemble baseline, the isotropic calibration parameter σ^2 is fit on the validation set and then fixed for test evaluation. **Best results are highlighted in bold.**

Method	Avg. MAE (kcal/mol/Å) \downarrow	Energy Score \downarrow	Coverage@95 ≈ 0.95	Calibration Error \downarrow	NLL \downarrow	Inference Time per-atom (ms) \downarrow
Ensemble(raw)	0.386 \pm 0.012	0.64 \pm 0.00	0.255	0.380	237.62	0.463 \pm 0.067
Ensemble(cal)	0.386 \pm 0.012	0.67 \pm 0.00	0.931	0.256	2.74	0.463 \pm 0.067
e²IP (Ours)	0.471 \pm 0.010	0.68 \pm 0.02	0.910 \pm 0.024	0.114 \pm 0.028	1.31 \pm 0.03	0.102 \pm 0.016

veal qualitative differences beyond point error. Ensemble(raw) is severely overconfident (reliability/PIT), leading to extremely low Coverage@95 and extremely large NLL, indicating that its raw uncertainty is not directly usable in practice. Ensemble(cal) reduces global overconfidence via isotropic scaling, but a single scalar cannot capture the configuration-dependent and orientation-specific error structure in condensed phases. In contrast, e²IP predicts a full covariance tensor end-to-end, explicitly modeling anisotropic and correlated uncertainty in 3D force space; this yields markedly better probabilistic consistency (lower NLL and CE/PIT) and fewer high-confidence-but-wrong predictions, making it more suitable for uncertainty-weighted simulation. Fig. 2 further shows stronger alignment between predicted epistemic scale and true force error, directly improving ranking-based decisions such as active learning (Kulichenko et al., 2023; Jung et al., 2024).

Although e²IP scores slightly lower on ES and Coverage@95, the high score of Ensemble(cal) depends on calibration, while the uncalibrated Ensemble(raw) only achieves 0.255 on this metric. Additionally, calibration also results in a slight increase in ES for Ensemble. Considering the Spearman correlation, CE, and NLL metrics, where e²IP significantly outperforms ensembles, we find that e²IP offers a more favorable accuracy–efficiency–reliability balance for uncertainty-aware MD workflows.

4.2. Sample Efficiency with Equivariance

We then evaluate sample efficiency on two molecular systems from the MD22 dataset, *Buckyball-Catcher* (C_{60} – C_{60}) and *Double-walled carbon nanotubes* (DWCT), which feature long-range and collective interactions and are more challenging than other MD22 molecules. We compare e²IP against two non-equivariant baselines: eIP (Xu et al., 2025) and *Ours w/o equiv.*, an ablation that preserves the same likelihood objective (NLL) and uncertainty regularization but removes rotational equivariance by constructing a non-equivariant Σ_0 via a Cholesky parameterization. All methods are trained using 30%, 50%, 70%, and 100% of the training data. Fig. 3 reports force MAE and Spearman rank

correlation as a function of training-set usage, capturing absolute accuracy and ranking quality, respectively.

Across both systems, e²IP consistently exhibits improved data efficiency, with the largest and most uniform gains on DWCT. This behavior aligns with the strong geometric anisotropy and extended interactions in nanotube systems, where enforcing rotational equivariance provides a powerful inductive bias that improves generalization under limited data. Removing equivariance (*Ours w/o equiv.*) degrades performance despite sharing the same training objective, indicating that the gains are not driven solely by the loss design. On *Buckyball-Catcher*, e²IP also improves sample efficiency, although the margin is less pronounced. We note that e²IP maintains stable Spearman correlation as data decreases, suggesting that it preserves relative force ordering while improving accuracy. We further probe this inductive bias by evaluating on randomly rotated DWCT test configurations, where equivariance becomes essential and e²IP achieves a larger margin.

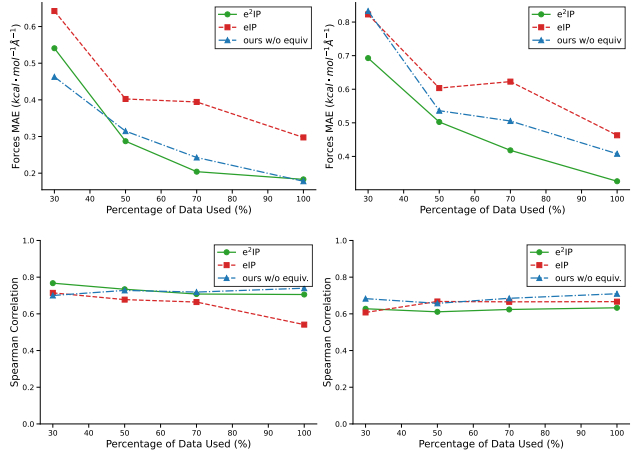


Figure 3. Data efficiency on MD22 subsets. Force MAE (top; lower is better) and Spearman rank correlation (bottom; higher is better) on *Buckyball-Catcher* (left) and DWCT (right) as a function of training-set usage (30/50/70/100%). We compare e²IP with eIP (Xu et al., 2025) and *Ours w/o equiv.*. e²IP achieves consistently lower MAE across data regimes, with the largest gains on DWCT, while maintaining stable rank correlation.

A physically meaningful force field should be *objective* under rigid-body rotations: rotating the coordinates by R should rotate the forces by the same R . To explicitly probe this property, we evaluate robustness under *proper* 3D rotations from the special orthogonal group

$$SO(3) = \{R \in \mathbb{R}^{3 \times 3} \mid R^\top R = I, \det(R) = +1\}.$$

Given a configuration with coordinates of atom i \vec{x}_i and reference forces \vec{f}_i , we construct a rotated input $\vec{x}'_i = R\vec{x}_i$ and the correspondingly rotated labels $\vec{f}'_i = R\vec{f}_i$. We then compute the force error magnitude $e_i = \|\vec{f}'_i - \hat{f}_i(\vec{x}'_i)\|$, and an uncertainty score u_i obtained from a rotationally invariant scalar proxy of the predicted uncertainty tensor (Eq. (15)). To assess whether uncertainty remains *actionable* after transformation, we measure the Spearman rank correlation between uncertainty and error, $\rho = \text{Spearman}(\{u_i\}, \{e_i\})$, report correlations on the original test set (ρ_{orig}) and the rotated test set (ρ_{rot}), and summarize the stability via $\Delta\rho = \rho_{\text{rot}} - \rho_{\text{orig}}$, where values closer to zero indicate better preservation of error–uncertainty alignment.

We focus on DWCT, where equivariance is expected to be particularly beneficial due to pronounced geometric anisotropy and extended interactions. For each DWCT test configuration, we sample an independent random $R \in SO(3)$ to form a rotated test set, and compare e²IP against eIP and the non-equivariant ablation *Ours w/o equiv.*. This setup isolates whether enforcing rotational equivariance improves transformation consistency and, critically, whether it preserves uncertainty-aware ranking under arbitrary 3D rotations.

Table 2 reports $\Delta\rho$ across different training-data regimes. Applying random $SO(3)$ rotations causes a modest degradation in rank alignment for all methods, which is reasonable in practice: even when the target mapping is equivariant, finite numerical precision and common implementation choices (e.g., discretization, neighbor selection, and approximate geometric features) can introduce small rotation-dependent perturbations. We further verify that our method satisfies $SO(3)$ equivariance to numerical precision; see Appendix H for details. Importantly, the non-equivariant baseline eIP exhibits the largest negative shifts, indicating that its uncertainty ranking is most sensitive to rotations. The ablation *Ours w/o equiv.* is more stable than eIP, suggesting that matching the likelihood objective and uncertainty regularization helps, but it still shows noticeably larger changes than e²IP. Across all data regimes, e²IP consistently achieves the smallest $|\Delta\rho|$ (Table 2), demonstrating that enforcing rotational equivariance is crucial for maintaining uncertainty–error alignment under arbitrary 3D rotations and thus for reliable, uncertainty-driven ranking in downstream use.

4.3. Backbone-migration Evaluation on SILICA Glass (OOD)

To stress-test the backbone-migration capability of our uncertainty head, we run controlled experiments on the SILICA glass benchmark (Tan et al., 2023) using another equivariant backbone PAiNN (Schütt et al., 2021) as the base predictor. We keep the PAiNN backbone and all training hyperparameters fixed across runs, and train different UQ heads with the *same random seed* to minimize variance from initialization (full settings in Appendix A). A key aspect of this benchmark is that the official test split is intentionally *out-of-distribution (OOD)*: training structures are generated under low temperature and low deformation rate, whereas test structures come from higher-temperature and higher-deformation-rate trajectories. This shift probes whether a UQ method remains informative when generalization is genuinely difficult, rather than under an in-domain split.

Following the dataset protocol, we subsample 1000 structures from the available training pool for training and use the remaining training structures for validation; evaluation is performed on the OOD test set. Table 3 reports force MAE together with the rank correlation between per-structure force RMSE and predicted uncertainty, where higher correlation indicates better uncertainty–error alignment for decision-making. Across both metrics, e²IP improves over the eIP baseline, demonstrating that our uncertainty head transfers effectively to a different backbone and remains useful under a challenging distribution shift.

Table 3. Results on the SILICA test set (OOD). We report force MAE and the spearman correlation coefficient between force RMSE and predicted uncertainty (higher is better). **Best results** are highlighted in **bold**.

Method	Forces MAE \downarrow	$\rho \uparrow$
eIP (Xu et al., 2025)	1.69	0.7603
e²IP (Ours)	1.49	0.7759

4.4. Ablation Study: Necessity of Spectral Stabilization

Our method constructs the base covariance Σ_0 during training, which must remain positive definite and numerically well-conditioned to support stable optimization (e.g., Cholesky factorization). To isolate the role of the proposed damper, we ablate the spectral stabilization while keeping all other components unchanged on the liquid water dataset from Sec. 4.1. The collapse behavior without spectral stabilization is consistently observed across other benchmarks, suggesting that the instability is a general numerical issue.

Figure 4 monitors the batch-wise mean and min–max band of the condition proxy $\lambda_{\max}(\Sigma_0)/\lambda_{\min}(\Sigma_0)$ over early training. With damping (left), the ratio may increase during ini-

Table 2. Change in Spearman correlation under random $SO(3)$ rotations on DWCT. We report $\Delta\rho = \rho_{\text{rot}} - \rho_{\text{orig}}$ (closer to 0 is better). Best results are highlighted in bold.

Method	30%	50%	70%	100%	Avg.
eIP (Xu et al., 2025)	-0.0856	-0.1454	-0.1302	-0.1418	-0.1258
$e^2\text{IP}$ (Ours) w/o equiv	-0.0754	-0.0384	-0.0449	-0.0432	-0.0505
$e^2\text{IP}$ (Ours)	-0.0470	-0.0235	-0.0244	-0.0008	-0.0239

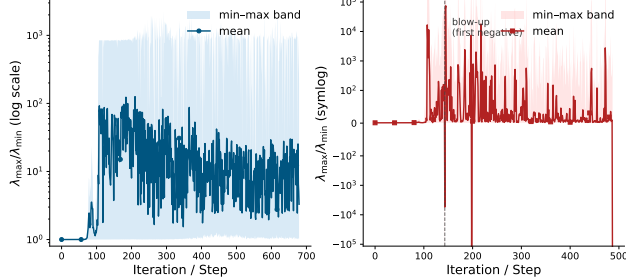


Figure 4. **Spectral stabilization is necessary for numerical robustness.** We track the batch-wise mean and min–max band of the eigenvalue ratio $\lambda_{\max}(\Sigma_0)/\lambda_{\min}(\Sigma_0)$ during early training. *left* (w/ damper): the ratio stays bounded and training remains stable. *right* (w/o damper): the ratio rapidly explodes and becomes erratic; negative values indicate that $\lambda_{\min}(\Sigma_0)$ turns non-positive due to finite-precision effects, after which Cholesky factorization fails (dashed line).

tial adaptation but quickly enters a bounded regime, and the min–max band remains controlled, indicating that the covariance spectrum stays well-conditioned throughout training.

Without damping (right), the spectrum becomes unstable: the eigenvalue ratio grows by orders of magnitude and fluctuates sharply across samples, signaling severe ill-conditioning. Moreover, the ratio can become negative, which implies $\lambda_{\min}(\Sigma_0) \leq 0$ and therefore a loss of positive definiteness under finite precision. After the first such event (dashed line), Cholesky factorization fails and training diverges. Overall, this ablation shows that spectral stabilization is not merely a convenience but a necessary component for reliable covariance construction in practice.

5. Discussion and Conclusion

Discussion. We introduced *Equivariant Evidential Deep Learning for Interatomic Potentials* ($e^2\text{IP}$), a single forward pass evidential framework for uncertainty estimation in vector-valued force fields. By representing predictive uncertainty as a full 3×3 SPD covariance, $e^2\text{IP}$ captures directional structure and cross-axis correlations that scalarized formulations cannot express. More broadly, our results indicate that geometric structure plays a direct role not only in predictive accuracy, but also in making uncertainty probabilistically interpretable and actionable for downstream decision-making in molecular simulation.

A central design principle of $e^2\text{IP}$ is to couple evidential learning with $SE(3)$ -equivariant rank-2 tensor modeling, ensuring that uncertainty transforms consistently under rotations. This is realized through a Lie-algebraic covariance parameterization, in which a symmetric matrix is mapped to the SPD manifold via the matrix exponential, providing positive definiteness by construction and aligning naturally with equivariant features. Our ablations further highlight an important practical consideration: learning full covariances can lead to numerical instability under finite precision if the spectrum becomes extreme. The proposed spectral damping and evidence regularization mitigate this issue, stabilizing training and improving calibration and error–uncertainty alignment.

Finally, because the uncertainty head operates on equivariant features and outputs structured tensor components, it can be integrated with different equivariant backbones with minimal modification. This backbone-agnostic design lowers the barrier to adopting structured uncertainty modeling in existing MLIP pipelines.

Limitations and Future Work. Our evaluation primarily targets $SO(3)$ consistency; extending to $O(3)$ (including reflections) and stress-testing under more extreme non-equilibrium conditions are natural next steps. In addition, the Normal-Inverse-Wishart prior may be restrictive under heavy-tailed residuals; richer priors (e.g., mixtures or robust alternatives) could further improve reliability. An important direction is to quantify downstream gains in uncertainty-aware molecular simulation, such as end-to-end active learning loops and stability improvements in long-timescale MD simulations.

Conclusion. We presented $e^2\text{IP}$, an $SE(3)$ -equivariant evidential framework that models aleatoric and epistemic uncertainty in atomic forces via full SPD covariances. Across molecular dynamics benchmarks, $e^2\text{IP}$ consistently outperforms baselines in uncertainty reliability and calibration quality, while achieving competitive predictive accuracy at single-model inference cost.

These results suggest that incorporating symmetry and tensor structure into uncertainty modeling is a principled and practical alternative to ensembling for uncertainty-aware molecular simulation.

References

- Abe, T., Buchanan, E. K., Pleiss, G., Zemel, R., and Cunningham, J. P. Deep ensembles work, but are they necessary? *Advances in Neural Information Processing Systems*, 35:33646–33660, 2022.
- Amini, A., Schwarting, W., Soleimany, A., and Rus, D. Deep evidential regression. In *Advances in Neural Information Processing Systems*, volume 33, pp. 14927–14937, 2020.
- Batista, I., Kovacs, D. P., Simm, G., Ortner, C., and Csanyi, G. Mace: Higher order equivariant message passing neural networks for fast and accurate force fields. In *Advances in Neural Information Processing Systems*, volume 35, pp. 11423–11436, 2022.
- Batzner, S., Musaelian, A., Sun, L., Geiger, M., Mailoa, J. P., Kornbluth, M., Molinari, N., Smidt, T. E., and Kozinsky, B. E(3)-equivariant graph neural networks for data-efficient and accurate interatomic potentials. *Nature Communications*, 13(1):2453, 2022.
- Behler, J. and Parrinello, M. Generalized neural-network representation of high-dimensional potential-energy surfaces. *Physical Review Letters*, 98(14):146401, 2007. doi: 10.1103/PhysRevLett.98.146401.
- Bilbrey, J. A., Firoz, J. S., Lee, M.-S., and Choudhury, S. Uncertainty quantification for neural network potential foundation models. *npj Computational Materials*, 11(1): 109, 2025.
- Cheng, B., Engel, E. A., Behler, J., Dellago, C., and Ceriotti, M. Ab initio thermodynamics of liquid and solid water. *Proceedings of the National Academy of Sciences*, 116 (4):1110–1115, 2019.
- Deng, D., Chen, G., Yu, Y., Liu, F., and Heng, P.-A. Uncertainty estimation by fisher information-based evidential deep learning. In *International conference on machine learning*, pp. 7596–7616. PMLR, 2023.
- Dern, N., Cunningham, J. P., and Pleiss, G. Theoretical limitations of ensembles in the age of overparameterization. *arXiv preprint arXiv:2410.16201*, 2024.
- Fu, X., Wu, Z., Wang, W., Xie, T., Keten, S., Gomez-Bombarelli, R., and Jaakkola, T. Forces are not enough: Benchmark and critical evaluation for machine learning force fields with molecular simulations. *Transactions on Machine Learning Research*.
- Gal, Y. and Ghahramani, Z. Dropout as a bayesian approximation: Representing model uncertainty in deep learning. In *International Conference on Machine Learning*, pp. 1050–1059. PMLR, 2016.
- Gasteiger, J., Shuaibi, M., Sriram, A., Günemann, S., Ulissi, Z. W., Zitnick, C. L., and Das, A. Gemnet-oc: Developing graph neural networks for large and diverse molecular simulation datasets. *Transactions on Machine Learning Research*.
- Gneiting, T. and Raftery, A. E. Strictly proper scoring rules, prediction, and estimation. *Journal of the American statistical Association*, 102(477):359–378, 2007.
- Jia, W., Wang, H., Chen, M., Lu, D., Lin, L., Car, R., Weinan, E., and Zhang, L. Pushing the limit of molecular dynamics with ab initio accuracy to 100 million atoms with machine learning. In *SC20: International conference for high performance computing, networking, storage and analysis*, pp. 1–14. IEEE, 2020.
- Jung, G. S., Choi, J. Y., and Lee, S. M. Active learning of neural network potentials for rare events. *Digital Discovery*, 3(3):514–527, 2024.
- Kozinsky, B., Musaelian, A., Johansson, A., and Batzner, S. Scaling the leading accuracy of deep equivariant models to biomolecular simulations of realistic size. In *Proceedings of the International Conference for High Performance Computing, Networking, Storage and Analysis*, pp. 1–12, 2023.
- Kulichenko, M., Barros, K., Lubbers, N., Li, Y. W., Messerly, R., Tretiak, S., Smith, J. S., and Nebgen, B. Uncertainty-driven dynamics for active learning of interatomic potentials. *Nature computational science*, 3(3): 230–239, 2023.
- Lakshminarayanan, B., Pritzel, A., and Blundell, C. Simple and scalable predictive uncertainty estimation using deep ensembles. In *Advances in Neural Information Processing Systems*, volume 30, 2017.
- Meinert, N. and Lavin, A. Multivariate deep evidential regression, 2021.
- Musaelian, A., Batzner, S., Johansson, A., Sun, L., Owen, C. J., Kornbluth, M., and Kozinsky, B. Learning local equivariant representations for large-scale atomistic dynamics. *Nature Communications*, 14(1):579, 2023.
- Perez, D., Subramanyam, A. P., Maliyov, I., and Swinburne, T. D. Uncertainty quantification for misspecified machine learned interatomic potentials. *npj Computational Materials*, 11(1):263, 2025.
- Rahaman, R. et al. Uncertainty quantification and deep ensembles. *Advances in neural information processing systems*, 34:20063–20075, 2021.
- Schütt, K., Unke, O., and Gastegger, M. Equivariant message passing for the prediction of tensorial properties

and molecular spectra. In *International Conference on Machine Learning*, pp. 9377–9388. PMLR, 2021.

Sensoy, M., Kaplan, L., and Kandemir, M. Evidential deep learning to quantify classification uncertainty. In *Advances in Neural Information Processing Systems*, volume 31, 2018.

Shumaylov, Z., Zaika, P., Rowbottom, J., Sherry, F., Weber, M., and Schönlieb, C.-B. Lie algebra canonicalization: Equivariant neural operators under arbitrary lie groups. In *The Thirteenth International Conference on Learning Representations*.

Soleimany, A. P., Amini, A., Goldman, S., Rus, D., Bhatia, S. N., and Coley, C. W. Evidential deep learning for guided molecular property prediction and discovery. *ACS Central Science*, 7(8):1356–1367, 2021. doi: 10.1021/acscentsci.1c00546.

Tan, A. R., Urata, S., Goldman, S., Dietschreit, J. C., and Gómez-Bombarelli, R. Single-model uncertainty quantification in neural network potentials does not consistently outperform model ensembles. *npj Computational Materials*, 9(1):225, 2023.

Thomas, N., Smidt, T., Kearnes, S., Yang, L., Li, L., Kohlhoff, K., and Riley, P. Tensor field networks: Rotation- and translation-equivariant neural networks for 3d point clouds, 2018.

Willow, S. Y., Park, T. H., Sim, G. B., Moon, S. W., Min, S. K., Yang, D. C., Kim, H. W., Lee, J., and Myung, C. W. Bayesian e (3)-equivariant interatomic potential with iterative restratification of many-body message passing. *arXiv preprint arXiv:2510.03046*, 2025.

Wollschläger, T., Gao, N., Charpentier, B., Ketata, M. A., and Günemann, S. Uncertainty estimation for molecules: Desiderata and methods. In *International conference on machine learning*, pp. 37133–37156. PMLR, 2023.

Wood, B. M., Dzamba, M., Fu, X., Gao, M., Shuaibi, M., Barroso-Luque, L., Abdelmaqsoud, K., Gharakhanyan, V., Kitchin, J. R., Levine, D. S., et al. Uma: A family of universal models for atoms. *arXiv preprint arXiv:2506.23971*, 2025.

Xu, H., Cui, T., Tang, C., Ma, J., Zhou, D., Li, Y., Gao, X., Gong, X., Ouyang, W., Zhang, S., et al. Evidential deep learning for interatomic potentials. *Nature Communications*, 2025.

Yin, B., Wang, J., Du, W., Wang, P., Ying, P., Jia, H., Zhang, Z., Du, Y., Gomes, C., Duan, C., et al. Alphanet: scaling up local-frame-based neural network interatomic potentials. *npj Computational Materials*, 11(1):332, 2025.

6. Impact Statements

This paper presents work whose goal is to advance the field of Machine Learning. We do not anticipate immediate negative societal impacts.

A. Additional details for e²IP

Table 4 summarizes the hyperparameters used for the AlphaNet and PAINN backbones in our experiments. Both models share the same optimization strategy and loss weighting scheme.

Table 4. Hyperparameters for AlphaNet and PAINN models used in experiments.

Category	Hyperparameter	AlphaNet	PAINN
Optimization	Optimizer	AdamW	
	Learning Rate	2×10^{-4}	
	Betas	(0.9, 0.999)	
	Weight Decay	0.0	
	Scheduler	ReduceLROnPlateau (min)	
Architecture	Factor / Patience	0.85 / 50	
	Number of Layers	4	6
	Cutoff Radius (r_c)	5.0 Å	5.0 Å
	Hidden Channels	128	128
	Num. Radial Basis	64	128
	Main χ_1 / MP χ_1	32 / 32	–
	χ_2	8	–
Loss & Reg.	Hidden Channels (χ)	96	–
	Energy Weight	1.0	
	Force Weight	10000.0	
	Evidence Reg. (λ_{reg})	0.1	

B. Notation and validity conditions

Table 5 summarizes symbols used in e²IP.

Table 5. Detailed Notation and Physical Interpretations used in e²IP.

Symbol	Mathematical Name	Physical Interpretation & Intuition
Input, Target & Latent Variables		
$\vec{y}_i \in \mathbb{R}^3$	Target Vector	The ground truth atomic force derived from DFT calculations on atom i .
$\vec{\mu}_i \in \mathbb{R}^3$	Latent Mean	The unknown "true" mean force. In the evidential framework, this is treated as a random variable following a Normal distribution.
$\Sigma_i \in \mathbb{S}_{++}^3$	Latent Covariance	The unknown "true" covariance of the aleatoric noise. It is treated as a random variable following an Inverse-Wishart distribution.
d	Dimension	The dimensionality of the target vector ($d = 3$ for atomic forces).
Evidential Parameters (Network Outputs)		
$\vec{\gamma}_i \in \mathbb{R}^3$	Evidential Mean	The model's best prediction for the atomic force. It serves as the mean of the predictive Student-t distribution.
$\Sigma_{0,i} \in \mathbb{S}_{++}^3$	Nominal Covariance	A symmetric positive definite matrix determining the shape of the aleatoric uncertainty. It captures directional correlations in force noise.
$\nu_i \in \mathbb{R}^+$	Degrees of Freedom of IW distribution	Represents the quantity of evidence supporting the estimated covariance shape $\Sigma_{0,i}$. Higher ν_i means the model is more confident about the aleatoric noise profile.
$\kappa_i \in \mathbb{R}^+$	Belief Count	Represents the quantity of evidence supporting the mean prediction $\vec{\gamma}_i$. Higher κ_i implies lower epistemic uncertainty (i.e., the model has seen ample similar training data).

Continued on next page...

Table 5 – continued from previous page

Symbol	Mathematical Name	Physical Interpretation & Intuition
$\Psi_i \in \mathbb{S}_{++}^3$	Scale Matrix	The scale matrix for the Inverse-Wishart prior, reparameterized as $\Psi_i = \nu_i \Sigma_{0,i}$ for physical interpretability.
Uncertainty Quantification Measures		
$U_{ale} \in \mathbb{S}_{++}^3$	Aleatoric Uncertainty	Expected data noise ($\mathbb{E}[\Sigma_i]$). It captures irreducible variability (e.g., thermal fluctuations) and transforms as a rank-2 tensor.
$U_{epi} \in \mathbb{S}_{++}^3$	Epistemic Uncertainty	Model uncertainty ($\text{Var}[\vec{\mu}_i]$). It captures the lack of knowledge in OOD regions. Computed as $\frac{\nu_i \Sigma_{0,i}}{\kappa_i(\nu_i - d - 1)}$.
m_i	DoF of t-distribution	Degrees of freedom for the posterior Student-t distribution, defined as $m_i = \nu_i - d + 1$.
Geometry, Lie Algebra & Optimization		
$\mathcal{S}_i \in \mathfrak{sym}(3)$	Lie Algebra Element	A symmetric matrix in the linear Lie algebra space. The network predicts this unbounded tensor to ensure unconstrained optimization.
$\exp(\mathcal{S}_i)$	Matrix Exponential	The map $\mathfrak{sym}(3) \rightarrow \mathbb{S}_{++}^3$ that transforms \mathcal{S}_i into the valid SPD covariance $\Sigma_{0,i}$, guaranteeing positive definiteness and equivariance by construction.
α_i	Spectral Damper	A scalar coefficient used to damp the magnitude of the traceless part of \mathcal{S}_i during training, preventing numerical instability (ill-conditioning).
\mathcal{L}_{NLL}	Negative Log-Likelihood	The primary loss function based on the multivariate Student-t distribution, encouraging accuracy and calibration.
\mathcal{L}_{reg}	Evidence Regularizer	A penalty term that discourages the model from assigning high evidence (ν_i, κ_i) to data points with large prediction errors.

Validity conditions. The predictive Student- t has positive degrees of freedom when $m_i = \nu_i - d + 1 > 0$, i.e., $\nu_i > d - 1$. In the main text we additionally require $\nu_i > d + 1$ so that $\mathbb{E}[\Sigma_i]$ exists and the tensor uncertainty decomposition in Eq. (8) is well-defined.

C. Derivation of the multivariate Student- t NLL

This appendix derives the expanded negative log-likelihood used in Eq. (13) in the main text, starting from the NIW predictive distribution.

C.1. Predictive Student- t from an NIW prior

Let $\vec{y}_i \in \mathbb{R}^d$ denote the target vector and let the likelihood be

$$p(\vec{y}_i \mid \vec{\mu}_i, \Sigma_i) = \mathcal{N}(\vec{y}_i \mid \vec{\mu}_i, \Sigma_i). \quad (16)$$

We place a Normal–Inverse–Wishart (NIW) prior on $(\vec{\mu}_i, \Sigma_i)$ with parameters $(\vec{\gamma}_i, \kappa_i, \Psi_i, \nu_i)$:

$$\Sigma_i \sim \mathcal{W}^{-1}(\Psi_i, \nu_i), \quad \vec{\mu}_i \mid \Sigma_i \sim \mathcal{N}\left(\vec{\gamma}_i, \frac{1}{\kappa_i} \Sigma_i\right), \quad (17)$$

where $\kappa_i > 0$ and $\nu_i > d - 1$ so that the predictive degrees of freedom are positive.

Marginalizing $(\vec{\mu}_i, \Sigma_i)$ yields a multivariate Student- t predictive distribution:

$$p(\vec{y}_i \mid \vec{\gamma}_i, \kappa_i, \Psi_i, \nu_i) = St_{\nu_i - d + 1}\left(\vec{y}_i \mid \vec{\gamma}_i, \frac{1 + \kappa_i}{\kappa_i(\nu_i - d + 1)} \Psi_i\right). \quad (18)$$

C.2. NLL in a log-determinant form

An equivalent closed form for the negative log-likelihood is

$$\begin{aligned}\mathcal{L}_{\text{NLL},i} &= \log \Gamma\left(\frac{\nu_i - d + 1}{2}\right) - \log \Gamma\left(\frac{\nu_i + 1}{2}\right) + \frac{d}{2} \log\left(\pi \frac{1 + \kappa_i}{\kappa_i}\right) - \frac{\nu_i}{2} \log |\Psi_i| \\ &\quad + \frac{\nu_i + 1}{2} \log \left| \Psi_i + \frac{\kappa_i}{1 + \kappa_i} (\vec{y}_i - \vec{\gamma}_i)(\vec{y}_i - \vec{\gamma}_i)^\top \right|.\end{aligned}\quad (19)$$

C.3. Reparameterization $\Psi_i = \nu_i \Sigma_{0,i}$

Following the main text (Eq. (6)), define $\Psi_i \triangleq \nu_i \Sigma_{0,i}$ with $\Sigma_{0,i}$ being a SPD matrix. Substituting into Eq. (19) gives

$$\begin{aligned}\mathcal{L}_{\text{NLL},i} &= \log \Gamma\left(\frac{\nu_i - d + 1}{2}\right) - \log \Gamma\left(\frac{\nu_i + 1}{2}\right) + \frac{d}{2} \log\left(\nu_i \pi \frac{1 + \kappa_i}{\kappa_i}\right) - \frac{\nu_i}{2} \log |\Sigma_{0,i}| \\ &\quad + \frac{\nu_i + 1}{2} \log \left| \Sigma_{0,i} + \frac{\kappa_i}{\nu_i(1 + \kappa_i)} (\vec{y}_i - \vec{\gamma}_i)(\vec{y}_i - \vec{\gamma}_i)^\top \right|.\end{aligned}\quad (20)$$

C.4. Determinant lemma and simplification

Define $\vec{v}_i \triangleq \vec{y}_i - \vec{\gamma}_i$ and $\alpha_i \triangleq \frac{\kappa_i}{\nu_i(1 + \kappa_i)}$. We apply the matrix determinant lemma:

$$|\mathbf{A} + \mathbf{u}\mathbf{u}^\top| = |\mathbf{A}| (1 + \mathbf{u}^\top \mathbf{A}^{-1} \mathbf{u}), \quad \text{for invertible } \mathbf{A}. \quad (21)$$

Setting $\mathbf{A} = \Sigma_{0,i}$ and $\mathbf{u} = \sqrt{\alpha_i} \vec{v}_i$ yields

$$|\Sigma_{0,i} + \alpha_i \vec{v}_i \vec{v}_i^\top| = |\Sigma_{0,i}| (1 + \alpha_i \vec{v}_i^\top \Sigma_{0,i}^{-1} \vec{v}_i). \quad (22)$$

Taking logarithms,

$$\log |\Sigma_{0,i} + \alpha_i \vec{v}_i \vec{v}_i^\top| = \log |\Sigma_{0,i}| + \log (1 + \alpha_i \vec{v}_i^\top \Sigma_{0,i}^{-1} \vec{v}_i). \quad (23)$$

Substituting Eq. (23) into Eq. (20), the $\log |\Sigma_{0,i}|$ terms combine as

$$-\frac{\nu_i}{2} \log |\Sigma_{0,i}| + \frac{\nu_i + 1}{2} \log |\Sigma_{0,i}| = \frac{1}{2} \log |\Sigma_{0,i}|. \quad (24)$$

Therefore we obtain the expanded form used in the main text:

$$\begin{aligned}\mathcal{L}_{\text{NLL},i} &= \log \Gamma\left(\frac{\nu_i - d + 1}{2}\right) - \log \Gamma\left(\frac{\nu_i + 1}{2}\right) + \frac{d}{2} \log\left(\frac{\pi \nu_i (1 + \kappa_i)}{\kappa_i}\right) + \frac{1}{2} \log |\Sigma_{0,i}| \\ &\quad + \frac{\nu_i + 1}{2} \log \left(1 + \frac{\kappa_i}{\nu_i(1 + \kappa_i)} (\vec{y}_i - \vec{\gamma}_i)^\top \Sigma_{0,i}^{-1} (\vec{y}_i - \vec{\gamma}_i)\right).\end{aligned}\quad (25)$$

D. Irrep-to-Cartesian map and the constant basis matrix \mathbf{Q}

This appendix specifies the implementation-dependent details omitted in Sec. 3.2. Let $\mathbf{z}_i = [s_i, \mathbf{t}_i] \in \mathbb{R}^{1+5}$ denote the coefficients in $(0e \oplus 2e)$. We map \mathbf{z}_i to a Cartesian symmetric matrix $\mathcal{S}_i \in \mathfrak{sym}(3)$ using a fixed Clebsch–Gordan basis.

One possible convention. We first produce a (not-necessarily symmetric) 3×3 matrix \mathbf{S}_i by a linear map,

$$\text{vec}(\mathbf{S}_i) = \mathbf{Q}^\top \mathbf{z}_i^\top, \quad \mathbf{Q} \in \mathbb{R}^{9 \times 6}, \quad (26)$$

where $\text{vec}(\cdot)$ stacks entries in a fixed order (e.g., row-major). We then symmetrize:

$$\mathcal{S}_i \triangleq \frac{1}{2} (\mathbf{S}_i + \mathbf{S}_i^\top) \in \mathfrak{sym}(3). \quad (27)$$

(Any equivalent convention that yields \mathcal{S}_i transforming as a rank-2 tensor is valid; we report the exact convention used in code for reproducibility.)

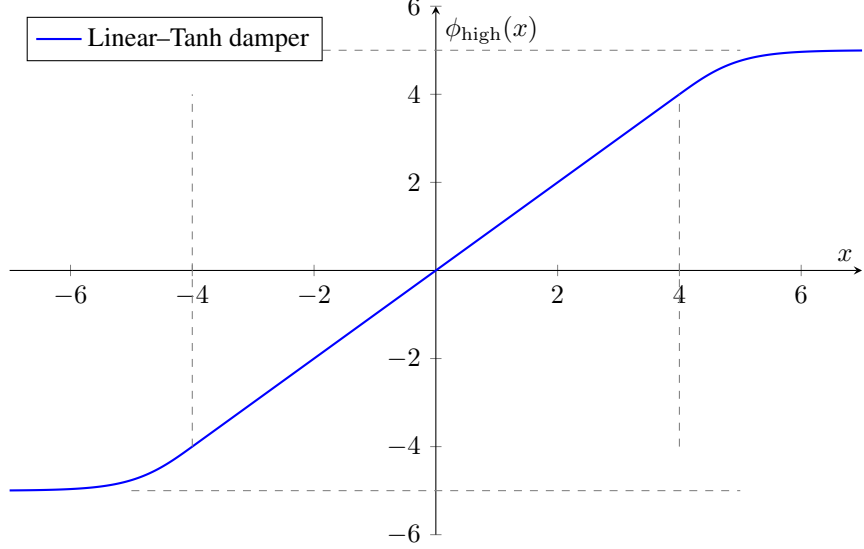


Figure 5. Linear-Tanh damping function with threshold $\tau = 4$ and ceiling $c = 5$. The mapping is linear near the origin and smoothly saturates for large inputs.

Equivariance. By construction of \mathbf{Q} from CG coefficients of $(1o \otimes 1o) \rightarrow (0e \oplus 2e)$, the resulting \mathcal{S}_i transforms as $\mathcal{S}_i \mapsto R\mathcal{S}_i R^\top$ for $R \in SO(3)$.

Implementation details. We utilized the `e3nn.io.CartesianTensor` method for this construction. Due to performance inefficiencies in the original source code, we re-implemented the transformation method and validated the consistency of our results against the original implementation.

E. Damping functions used for spectral stabilization

For completeness we provide the explicit damping used in Section 3.3.

Linear-Tanh damper. We define a smooth piecewise function that is linear near the origin and saturates to a ceiling:

$$\phi_{\text{high}}(x) = \begin{cases} x, & |x| \leq \tau, \\ \text{sgn}(x) \left[(c - \tau) \tanh\left(\frac{|x| - \tau}{c - \tau}\right) + \tau \right], & |x| > \tau, \end{cases} \quad (28)$$

with threshold τ and ceiling c . The lower damper ϕ_{low} is defined analogously to enforce a floor on the isotropic channel. In our experiment, we use $\tau = 4$ and $c = 5$.

Coefficient-space application. Scalar: $\tilde{s}_i = \phi_{\text{low}}(\phi_{\text{high}}(s_i))$. Vector: $\tilde{\mathbf{t}}_i = \alpha_i \mathbf{t}_i$ with α_i defined in Eq. (12).

F. Evaluation Metrics

We evaluate uncertainty quality for vector-valued force prediction using distribution-aware calibration diagnostics together with negative log-likelihood (NLL) and the multivariate Energy Score (ES). Each atom-level force is a 3D vector. For sample i , let the target and prediction be $y_i \in \mathbb{R}^3$ and $\mu_i \in \mathbb{R}^3$, and define the error

$$e_i = y_i - \mu_i \in \mathbb{R}^3. \quad (29)$$

Let $\Sigma_i \in \mathbb{R}^{3 \times 3}$ denote the predicted positive definite matrix used by the model. For the Gaussian baseline, Σ_i is the predictive covariance. For our Student- t model, we use the scale matrix Λ_i defined as

$$\Lambda_i = \frac{(1 + \kappa)\nu_i}{\kappa(\nu_i - d + 1)} \Sigma_i, \quad m_i := \nu_i - d + 1. \quad (30)$$

Predictive families. Our method (e²IP) outputs a multivariate Student- t predictive distribution with effective degrees of freedom m_i and scale matrix Λ_i :

$$e_i \sim St_{m_i}(0, \Lambda_i). \quad (31)$$

The deep ensemble baseline uses a Gaussian predictive distribution

$$e_i \sim \mathcal{N}(0, \Sigma_i). \quad (32)$$

where Σ_i is constructed from epistemic covariance plus an isotropic floor as described in the main text.

F.1. Distribution-aware Calibration Curve, Coverage, and Calibration Error

Calibration is assessed via the probability integral transform (PIT). For each method, we map the multivariate residual e_i to a scalar $u_i \in (0, 1)$ such that u_i is uniform when the predictive distribution is calibrated.

Gaussian baseline. For the ensemble Gaussian predictive model, define the squared Mahalanobis distance

$$m_i^2 = e_i^\top \Sigma_i^{-1} e_i. \quad (33)$$

If $e_i \sim \mathcal{N}(0, \Sigma_i)$ in 3D, then $m_i^2 \sim \chi_3^2$, and we set

$$u_i^{\text{Gauss}} = F_{\chi_3^2}(m_i^2), \quad (34)$$

where $F_{\chi_3^2}$ denotes the CDF of χ_3^2 . Under perfect calibration, $u_i^{\text{Gauss}} \sim \text{Unif}(0, 1)$.

Student- t model (ours). For our Student- t predictive model in 3D, we again use the quadratic form $m_i^2 = e_i^\top \Lambda_i^{-1} e_i$. If $e_i \sim t_{\nu_i-d+1}(0, \frac{(1+\kappa)\nu}{\kappa(\nu-d+1)} \Sigma_i)$, then the scaled statistic

$$x_i = \frac{m_i^2}{3} \quad (35)$$

follows an F distribution:

$$x_i \sim F(3, \nu_i - d + 1). \quad (36)$$

We therefore define the PIT for our method as

$$u_i^t = F_{F(3, \nu_i - d + 1)}\left(\frac{m_i^2}{3}\right), \quad (37)$$

where $F_{F(3, \nu_i - d + 1)}(\cdot)$ is the CDF of the $F(3, \nu_i)$ distribution. Under perfect calibration, $u_i^t \sim \text{Unif}(0, 1)$.

Unified calibration curve. Given a grid of nominal confidence levels $\mathcal{P} = \{p_1, \dots, p_M\} \subset (0, 1)$, we define the empirical (observed) coverage curve for any method as

$$\text{Obs}(p) = \frac{1}{N} \sum_{i=1}^N \mathbb{I}[u_i \leq p], \quad p \in \mathcal{P}, \quad (38)$$

where u_i is the PIT scalar computed using the method's own predictive family (Gaussian or Student- t). The ideal calibration curve satisfies $\text{Obs}(p) = p$.

Coverage at a nominal level. We report $\text{Coverage}@p^* = \text{Obs}(p^*)$ for selected nominal levels (e.g., $p^* \in \{0.8, 0.9, 0.95\}$). Values closer to p^* indicate better calibration at that confidence level.

Calibration error. We summarize deviation from the ideal curve using an ℓ_1 calibration error over the grid:

$$\text{CE}_{\ell_1} = \frac{1}{M} \sum_{m=1}^M |\text{Obs}(p_m) - p_m|. \quad (39)$$

F.2. Negative Log-Likelihood (Model-specific)

We report the average negative log-likelihood under each method's predictive distribution:

$$\text{NLL} = -\frac{1}{N} \sum_{i=1}^N \log p(e_i), \quad (40)$$

where $p(e_i)$ is the density of $\mathcal{N}(0, \Sigma_i)$ for the ensemble baseline and the density of $t_{m_i}(0, \Lambda_i)$ for our method. Since these correspond to different distribution families, NLL should be interpreted as a model-specific proper score.

F.3. Energy Score (Multivariate Proper Scoring Rule)

To assess the full multivariate predictive distribution in a distribution-agnostic manner, we compute the Energy Score (ES), a strictly proper scoring rule for multivariate forecasts. For a predictive random variable $X_i \sim F_i$ and an independent copy X'_i , the Energy Score is

$$\text{ES}_i = \mathbb{E} [\|X_i - y_i\|_2] - \frac{1}{2} \mathbb{E} [\|X_i - X'_i\|_2], \quad (41)$$

where F_i is the method's predictive distribution (Gaussian for the ensemble, Student- t for ours). Lower ES indicates better probabilistic predictions. We estimate the expectations via Monte Carlo with S samples:

$$\widehat{\text{ES}}_i = \frac{1}{S} \sum_{s=1}^S \|x_i^{(s)} - y_i\|_2 - \frac{1}{2} \cdot \frac{1}{S} \sum_{s=1}^S \|x_i^{(s)} - \tilde{x}_i^{(s)}\|_2, \quad (42)$$

$$x_i^{(s)} \stackrel{\text{i.i.d.}}{\sim} F_i, \quad \tilde{x}_i^{(s)} \stackrel{\text{i.i.d.}}{\sim} F_i. \quad (43)$$

We report the mean Energy Score over the evaluation set.

G. Ensemble Predictive Covariance and $\sigma^2 I$ Calibration

For a deterministic ensemble with member predictions $\{\mu_i^{(k)}\}_{k=1}^K$, we form the ensemble mean

$$\mu_i = \frac{1}{K} \sum_{k=1}^K \mu_i^{(k)}, \quad (44)$$

and an epistemic covariance estimate

$$\Sigma_i^{\text{epi}} = \frac{1}{K} \sum_{k=1}^K \left(\mu_i^{(k)} - \mu_i \right) \left(\mu_i^{(k)} - \mu_i \right)^\top. \quad (45)$$

To improve calibration, we optionally add an isotropic variance floor

$$\Sigma_i(\sigma^2) = \Sigma_i^{\text{epi}} + \sigma^2 I, \quad (46)$$

where $\sigma^2 \geq 0$ is fitted on a validation set by matching the observed coverage at a target level p_{target} (we use $p_{\text{target}} = 0.9$). Concretely, we choose σ^2 such that

$$\text{Obs}_{\text{val}}^{\sigma^2}(p_{\text{target}}) \approx p_{\text{target}}, \quad (47)$$

and then evaluate all metrics on the test set using the fixed σ^2 .

H. Equivariance Validation via Random Rotations

In this section, we provide a numerical validation of the rotational equivariance properties of the proposed model. Specifically, we verify that the predicted forces and uncertainty tensors transform correctly under arbitrary three-dimensional rotations.

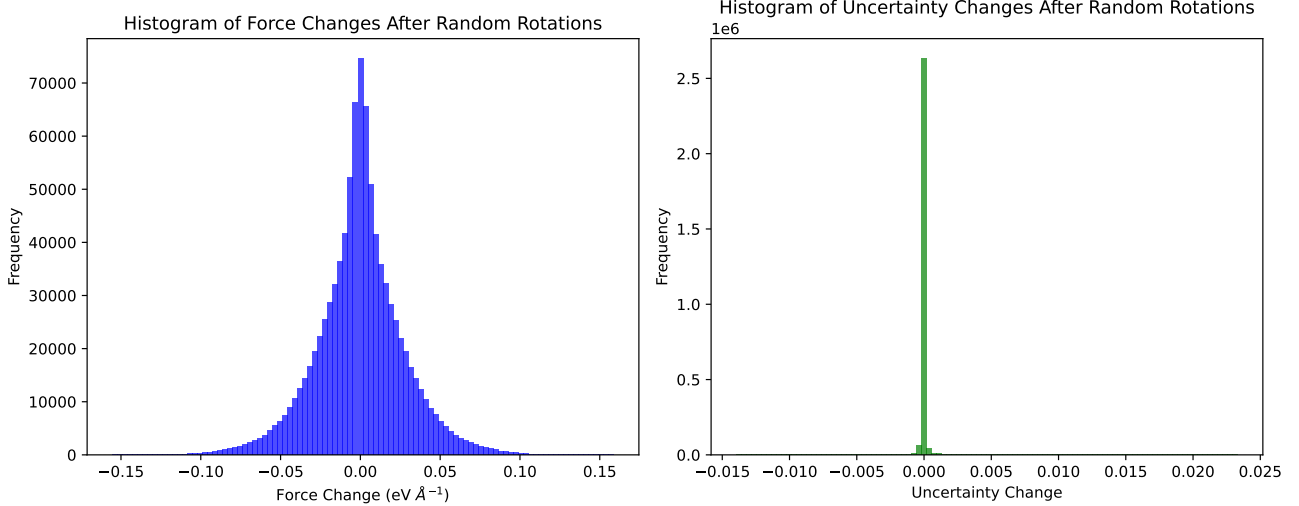


Figure 6. Histograms of deviations under random $\text{SO}(3)$ rotations for a representative DWCT structure. **Left:** force deviations $\mathbf{F}(Rx) - R\mathbf{F}(\mathbf{x})$. **Right:** uncertainty deviations $\Sigma(Rx) - R\Sigma(\mathbf{x})R^\top$. Both distributions are sharply peaked at zero, indicating that the model outputs satisfy rotational equivariance up to numerical precision.

H.1. Experimental setup

We randomly select a representative DWCT structure and apply a set of independent random rotations. For each trial, a rotation matrix $R \in \text{SO}(3)$ is sampled uniformly, and the atomic positions are transformed as $\mathbf{x} \mapsto Rx$.

Let $\mathbf{F}(\mathbf{x}) \in \mathbb{R}^{N \times 3}$ denote the predicted forces and let $\mathbf{U}_{epi}(\mathbf{x}) \in \mathbb{R}^{3 \times 3}$ denote the predicted uncertainty tensor. For each rotation, we compute the deviations

$$\Delta\mathbf{F} = \mathbf{F}(Rx) - R\mathbf{F}(\mathbf{x}), \quad (48)$$

and

$$\Delta\mathbf{U}_{epi} = \mathbf{U}_{epi}(Rx) - R\mathbf{U}_{epi}(\mathbf{x})R^\top. \quad (49)$$

The experiment is repeated for 300 randomly sampled rotations. All components of the resulting deviation tensors are collected and flattened to form empirical distributions.

H.2. Results

Figure 6 shows histograms of the force and uncertainty deviations. Both distributions are sharply centered around zero.

For the force predictions, the deviations exhibit a symmetric distribution with small variance, indicating that the vector-valued outputs satisfy rotational equivariance to numerical precision. For the uncertainty predictions, the deviations are even more tightly concentrated around zero, reflecting the stable equivariant behavior of the second-order tensor output.

The observed residual deviations are several orders of magnitude smaller than the typical scale of the model outputs and are attributed to floating-point rounding errors and accumulated numerical precision limits. These results confirm that the proposed model preserves $\text{SO}(3)$ equivariance for both force and uncertainty predictions in practice.